





Capillary driven fragmentation of large gas bubbles in turbulence

Aliénor Rivière ¹, Daniel J. Ruth,² Wouter Mostert ³,

Luc Deike ^{2,4} and Stéphane Perrard ^{1,5,*}

¹*Physique et Mécanique des Milieux Hétérogènes, CNRS, ESPCI Paris, University PSL, Paris 75005, France*

²*Department of Mechanical and Aerospace Engineering, Princeton University, Princeton, New Jersey 08544, USA*

³*Department of Engineering Science, University of Oxford, Oxford OX1 3PJ, United Kingdom*

⁴*High Meadows Environmental Institute, Princeton University, Princeton, New Jersey 08544, USA*

⁵*LPENS, Département de Physique, Ecole Normale Supérieure, PSL University, 75005 Paris, France*



(Received 11 June 2021; accepted 21 June 2022; published 30 August 2022)

The bubble size distribution below a breaking wave is of paramount interest when quantifying mass exchanges between the atmosphere and oceans. Mass fluxes at the interface are driven by bubbles that are small compared with the Hinze scale d_h , the critical size below which bubbles are stable, even though individually these are negligible in volume. Combining experimental and numerical approaches, we report a power-law scaling $d^{-3/2}$ for the small bubble size distribution, for sufficiently large separation of scales between the injection size and the Hinze scale. From an analysis of individual bubble breakups, we show that small bubbles are generated by capillary effects, and that their breakup time scales as $d^{3/2}$, which physically explains the sub-Hinze scaling observed.

DOI: [10.1103/PhysRevFluids.7.083602](https://doi.org/10.1103/PhysRevFluids.7.083602)

I. INTRODUCTION

Bubble fragmentation drives gas dissolution by drastically increasing the exchange surface between phases. For instance, up to 40% of the total CO_2 uptake by the ocean is due to bubble-mediated gas transfer [1–3]. More specifically, it is the bubble size distribution that controls gas transfer [4,5] and spray production as bubbles burst at the surface [6–9]. Bubbles also play a major role in industrial applications like oil and gas transportation from remote wells [10] or oil spill mitigation [11,12].

As a consequence, the fragmentation of bubbles has been extensively studied in model experiments [13–16] as well as under breaking waves both experimentally [17–20] and numerically [21–23]. For large bubbles, a consensus has been reached on the bubble size distribution, described as $\mathcal{N}(d) \propto d^{-10/3}$ with d being the bubble volume equivalent diameter. This law originates from a self-similar cascade of breakups [24], in which each bubble produces a fixed number of equally sized child bubbles, on a time given by the typical velocity fluctuations correlation time at the bubble scale d . This correlation time scales with the eddy turnover time $t_c(d) = \epsilon^{-1/3} d^{2/3}$ where ϵ is the averaged dissipation rate of kinetic energy by viscous dissipation, which is used to characterize turbulent flows [25].

The $\mathcal{N}(d) \propto d^{-10/3}$ scaling holds down to the Hinze scale d_h , the size at which kinetic energy balances surface-tension energy. The ratio of inertial and surface tension effects defines the Weber number, $We = \rho U^2 d / \gamma$, where γ is the liquid-gas surface tension, ρ is the liquid density, and U is a characteristic velocity driving the interface deformation. For a bubble immersed in a turbulent

*stephane.perrard@espci.fr

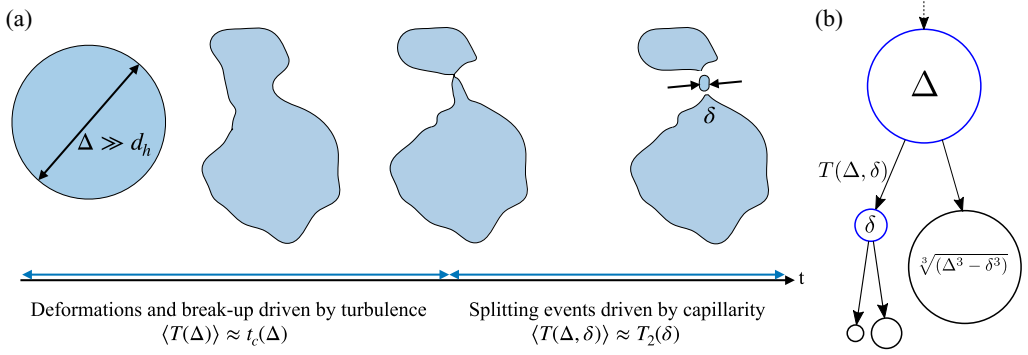


FIG. 1. (a) Sketch of a breakup process, involving inertial deformations, followed by a capillary splitting event. (b) Schematic of a bubble of size Δ splitting into a small bubble of size δ in a time $T(\Delta, \delta)$ and subsequent splittings.

flow, the characteristic velocity U is chosen as the averaged velocity difference at bubble bubble diameter scale. If the bubble is within the inertial range, i.e., where the turbulent fluctuations are scale invariant, the velocity increment is given by $\langle (\Delta u)^2 \rangle = 2\epsilon^{2/3} d^{2/3}$ [26], where $\langle \rangle$ denotes the average over realization, often called the ensemble-average operation. The average velocity increment at the bubble scale defines the Weber number for a bubble in a turbulent flow,

$$We = \frac{2\rho\epsilon^{2/3}d^{5/3}}{\gamma}. \quad (1)$$

Concomitantly, the Hinze scale d_h [27] separates stable bubbles ($d < d_h$) from those that will fragment ($d > d_h$),

$$d_h = \left(\frac{We_c}{2} \right)^{3/5} \left(\frac{\gamma}{\rho} \right)^{3/5} \epsilon^{-2/5}, \quad (2)$$

with We_c being the critical Weber number for breakup, which is typically an order one constant [14, 28, 29]. Note that due to the inherent stochasticity of turbulent flows, the Hinze scale d_h is a soft-breakup limit.

The sub-Hinze bubble size distribution ($d \ll d_h$) always exhibits a gentler slope than $\mathcal{N}(d) \propto d^{-10/3}$, although there is variability among the experimental studies [17–20], and the observations lack a physical explanation [18]. The difficulty arises from the large-scale separation between sub-Hinze bubbles and their parent size bubbles: the sub-Hinze distribution cannot be explained by a self-similar cascade process, so a different physical argument is required.

In this article, we describe the physical mechanism leading to the sub-Hinze size distribution resulting from the breakup of large super-Hinze bubbles. We decompose the bubble fragmentation dynamics by sequences of binary events and consider two concomitant processes: *breakup events*, akin to the inertial self-similar process [24] which lead to the formation of two bubbles of similar sizes, and *splitting events*, which creates one sub-Hinze and one super-Hinze bubble, largely separated in size. For large separation of scales between the initial cavity and the Hinze scale, the turbulence induces strong deformation, creating elongated structures, which will fragment on a timescale set by capillarity, much faster than the surrounding turbulence timescales. Figure 1 sketches the succession of the typical breakup and splitting events. Considering these two types of processes within a population balance equation and their associated timescale, we recover the two power-law scalings for the bubble size distribution with $\mathcal{N}(d) \propto d^{-10/3}$ for $d > d_h$ originating from self-similar breakup controlled by the eddy-turnover time at scale d , and $\mathcal{N}(d) \propto d^{-3/2}$ for $d < d_h$ controlled by capillary breakup time of ligaments of diameter d . To test the validity of our model, we

analyze individual splitting events using three-dimensional two-phase direct numerical simulations (DNS) of bubble breakup in turbulence. Next, we present an experiment that achieves a large-scale separation between an initial large bubble and the Hinze scale, which produces a clear sub-Hinze bubble size distribution power law $\mathcal{N}(d) \propto d^{-3/2}$, in accordance with the theoretical model and the numerical simulations.

II. MODEL OF SUB-HINZE BUBBLE PRODUCTION

Let consider the fragmentation dynamics as a succession of binary events and we neglect the correlation between successive events. Let $T(\Delta, \delta)$ denotes the lifetime of the parent bubble, of equivalent diameter Δ , which produces two child bubbles of equivalent diameters δ and $(\Delta^3 - \delta^3)^{1/3} \geq \delta$ (from volume conservation), as sketched in Fig. 1. For equal-size child bubbles we have $\delta = c\Delta$ with $c = 2^{-1/3} \approx 0.79$ a numerical constant.

The mean bubble flux $\Phi(\Delta, d, t)$ is the production rate of bubbles of diameter d from the breakup of a bubble of size Δ , and is decomposed into the product of a breakup rate $\omega(\Delta)$ and a child size probability density $f(\Delta, d)$ per unit of diameter and can be written as [30, Chap. 4, Eq. (2.1)], [31],

$$\Phi(\Delta, d, t) = 2f(\Delta, d)\omega(\Delta)\mathcal{N}(\Delta, t), \quad (3)$$

where $\mathcal{N}(\Delta, t)$ is the number density of bubbles of size Δ at time t , and the factor 2 comes from the assumption of binary events, which is discussed in greater details in Ref. [14,16,28,32]. The breakup rate $\omega(\Delta)$ is the average number of breakup events of bubble of size Δ per unit of time, also called breakup frequency. The probability density f is often referred to as the child bubble size distribution and is the probability density function for a child of size d given the breakup of a bubble of size Δ .

From Eq. (3), we obtain the temporal evolution of the bubble size distribution from the fragmentation of an initial bubble of size d_0 as the difference between a birth term and a death term [14]:

$$\frac{\partial \mathcal{N}(d, t)}{\partial t} = \int_d^{d_0} \Phi(\Delta, d, t) d\Delta - \omega(d)\mathcal{N}(d), \quad (4)$$

considering the total bubble size distribution in a spatially homogeneous configuration, henceforth neglecting the spatial advection terms. Equation (4) is the starting point of numerous population balance models.

For super-Hinze bubbles $d > d_h$, we recall the argument from [24]. Considering breakup rates controlled by the eddy turn-over time at the scale of the parent bubble, using (4) at steady state leads to $\mathcal{N}(d) \propto d^{-10/3}$ [23,24]. In this self similar model, a bubble of size d breaks, in a time given by $t_c(d) = \epsilon^{-1/3}d^{2/3}$, into m fragments of equal diameter $m^{-1/3}d$. Each of these child bubbles then breaks in a time $\epsilon^{-1/3}(m^{-1/3}d)^{2/3}$. We obtain an increasing number of $m \times m^{-2/9} = m^{7/9}$ bubbles per unit of time, which yields the bubble density $\mathcal{N}(m^{-1/3}d) = m^{1/3}m^{7/9}\mathcal{N}(d)$. Assuming $\mathcal{N}(d) \propto d^\alpha$, we have $-\alpha/3 = 1/3 + 7/9$ which gives $\alpha = -10/3$ [24]. For $d < d_h$, the self-similar argument cannot be applied anymore since surface tension must be important at this scale.

Here we propose a scaling for the sub-Hinze bubble size distribution, i.e., for $d < d_h$. In equation (3) the rate $\omega(\Delta)$ at which a bubble breaks up does not distinguish between processes which produce equally sized child bubbles or highly asymmetrically sized child bubbles, for which at least one child bubble is smaller than the Hinze scale. These two types of events, however, may occur on very different timescales. Here, we consider that the fragmentation statistics depends on both the parent size Δ and smallest child size δ , a framework that has been used previously for models based on bubble-eddy interactions [33]. We assume that the production of small bubbles ($d < d_h$) is controlled by bubble splitting events, in which elongated filaments become unstable under a Rayleigh-Plateau-like mechanism [34]. These elongated structures result from the deformation of larger bubbles due to the turbulent fluctuations, which occur at timescale controlled by the turbulence (as sketched in Fig. 1). Then, the time for such elongated filaments to rupture will be

controlled by capillarity, at the scale of the filament. This stems from the “freezing” in place of the turbulent flow relative to the accelerating collapse dynamics in the final moments before rupture, which was shown experimentally by Ruth *et al.* [35]. A cascade of splitting events leads to the formation of sub-Hinze bubbles, whose size δ are comparable to the diameter of the filament, and one larger bubble. The exact geometry of the filament and the splitting time varies from one realization to the other, but considering an ensemble average, the splitting time $T(\Delta, \delta)$ will be given by the capillary time $T_2(\delta)$ at size small δ :

$$\langle T(\Delta, \delta) \rangle = T_2(\delta) = \frac{1}{2\sqrt{3}} \left(\frac{\rho}{\gamma} \right)^{1/2} \delta^{3/2}, \quad (5)$$

where the capillary time $T_2(\delta)$ is the inverse of the angular frequency of oscillation of the principal mode of oscillation of an inviscid bubble in a quiescent fluid [36], and also correspond to the growth rate of Rayleigh plateau instability of a bubble filament [34]. When the capillary mechanism dominates, the bubble lifetime T scales as $\delta^{3/2}$, with δ being the size of the smallest child bubble, is independent of the parent size and will control the shape of the bubble size distribution.

While the two breakup mechanisms we consider are happening concomitantly, $O(10-100)$ splitting events follow a single breakup event for $d \gg d_h$, so that the capillary timescale dominates the production of sub-Hinze bubbles. We integrate the splitting events within the population balance framework and use flux conservation to express ω and f from equation (3) in terms of the newly introduced timescale:

$$f(\Delta, d)\omega(\Delta) = \frac{F(\Delta, \delta)}{\langle T(\Delta, \delta) \rangle} = \frac{F(\Delta, \delta)}{T_2(\delta)}, \quad (6)$$

with $\delta = d$ if the child bubble considered is the smaller one of the two produced (that is, if $d < c\Delta$) and $\delta = (\Delta^3 - d^3)^{1/3}$ if it is the larger of the two (that is, if $d > c\Delta$), since the production is controlled by the faster of the two timescales. Note that a bubble lifetime that depend on both the parent and the child bubble size was introduced by Wang *et al.* [33]. $F(\Delta, \delta)$ is the weight associated with each breakup frequency and can be interpreted as the likelihood of breakup of a bubble of size Δ into a bubble of size δ . We use DNS of bubble breakup in homogeneous and isotropic turbulence to estimate F and will find that $F(\Delta, \delta) \equiv F(\Delta)$ is independent of δ . Proving the independence of the weight factor $F(\Delta)$ on δ would require a complete analysis of the filament geometry, which is not accessible with our numerical dataset. The independence of F on δ could be attributed to the absence of a characteristic length scale in a turbulent flow, such that no specific filament size is selected. We will work with the assumption $F(\Delta)$ in the remaining of the theoretical discussion.

For $d < d_h$, using Eq. (6) in Eq. (4), we split the birth term into two parts, one term taking into account breaking for $\delta < c\Delta$ and one for $\delta > c\Delta$, and we obtain

$$\frac{\partial \mathcal{N}(d, t)}{\partial t} = \int_{d/c}^{d_0} 2 \frac{F(\Delta)}{T_2(d)} \mathcal{N}(\Delta, t) d\Delta + \int_d^{d/c} 2 \frac{F(\Delta)}{T_2(\sqrt{[3]\Delta^3 - d^3})} \mathcal{N}(\Delta, t) d\Delta - \omega(d) \mathcal{N}(d, t), \quad (7)$$

where d_0 is the largest bubble size in the system. Assuming that bubbles smaller than d_h do not break implies that the second integral and the death term vanish, and that the lower bound of the first integral is d_h leading to

$$\frac{\partial \mathcal{N}(d, t)}{\partial t} = \int_{d_h}^{d_0} 2 \frac{F(\Delta)}{T_2(d)} \mathcal{N}(\Delta, t) d\Delta. \quad (8)$$

Integrating over time, we obtain for $d < cd_h$

$$\mathcal{N}(d, t) = d^{-3/2} \int_0^t I_{\mathcal{N}}(d_0/d_h, s) ds, \quad (9)$$

with

$$I_{\mathcal{N}}(d_0/d_h, t) = \int_{d_h}^{d_0} 4\sqrt{3}F(\Delta) \left(\frac{\rho}{\gamma}\right)^{-1/2} \mathcal{N}(\Delta, t) d\Delta. \quad (10)$$

The integral $I_{\mathcal{N}}$ does not depend on the child bubble size d , so that the bubble size distribution for $d < cd_h$ follows

$$\mathcal{N}(d, t) \propto d^{-3/2}. \quad (11)$$

The details of the breakup cascade above the Hinze scale and its the temporal evolution only affects the total number of sub-Hinze bubbles produced while the scaling exponent $d^{-3/2}$ is not affected and is independent of time.

III. DIRECT NUMERICAL SIMULATIONS

To evaluate the validity of the physical arguments leading to $\mathcal{N}(d, t) \propto d^{-3/2}$, we perform DNS of a single initial bubble larger than the Hinze scale in a turbulent flow using the free software BASILISK [37,38]. A detailed description of the numerical configuration can be found in Rivière *et al.* [39]. We first create a homogeneous and isotropic turbulent flow at Taylor Reynolds number $Re_\lambda = 38$, following the method introduced by Rosales and Meneveau [40]. We then introduce a spherical bubble of diameter d_0 within the inertial range of the Kolmogorov cascade [26], i.e., at a scale where turbulence is scale invariant. The density ratio is $\rho/\rho_g = 850$ and the dynamical viscosity ratio is $\mu/\mu_g = 25$ where the subscript g refers to the gas phase located inside the bubble. We vary the ratio d_0/d_h and we have verified that the velocity statistics at the scale of the parent bubble are typical of turbulent flows [41] (although the Taylor Reynolds number is smaller than that in typical experimental conditions). We perform at least ten simulations per value of the initial bubble size d_0/d_h (2.9, 4.1, 5.2) with a spatial resolution of 135 points per diameter. We analyze the lifetime of all bubbles of diameter larger than four grid points.

Figure 2 presents snapshots of a large bubble (giving an initial separation of scales $d_0/d_h = 2.9$) subject to large deformations, described in detail in Rivière *et al.* [39]. The initial breakup, which occurs within one eddy turnover time at the bubble scale $t_c(d_0)$ [39], is followed by a rapid succession of splitting events, occurring on a much faster timescale and producing dozens of sub-Hinze-scale bubbles.

As previously, we decompose the dynamics into binary events and associate a lifetime $T(\Delta, \delta)$ to each parent bubble of size Δ producing a small child bubble of size δ . We compute the values of the equivalent diameters Δ and δ from parent and child bubble volumes. All individual bubbles are tracked from birth to death to determine $T(\Delta, \delta)$ using a reconstruction process of the full event sequence for each simulation. To do so, all individual bubbles are first tracked in space and time using the Python package TRACKPY [42] based on the Crocker-Grier algorithm [43]. Using volume and momentum conservation during breakup events, we reconstruct the breakage tree event by event. Each criterion has been manually adjusted and tested on simple situations to validate the algorithm robustness. The processing is systematically applied to the entire data set and leads to the identification of 4329 breaking events for d_0/d_h ranging from 2.9 to 5.2, using 78 different 3D DNS realizations of bubble breakup. In the following, we focus on the sub-Hinze bubble production, corresponding to $\delta < d_h$ and $t < 4t_c(d_0)$, during which most of the sub-Hinze bubbles are generated [39]. Given the low volume fraction of air, the coalescence events are statistically negligible.

Figure 3(a) shows the splitting times $T(\Delta, \delta)$ as a function of the size of the smallest child bubble they produce, δ . Each individual event is color coded by the parent size Δ , highlighting a broad distribution of splitting times, almost all smaller than the eddy turn-over time at the small child bubble's scale, $t_c(\delta)$. This suggests that these splitting events are not primarily instigated by turbulent deformations at the small child scale. To estimate the ensemble average $\langle T(\Delta, \delta) \rangle$ over multiple realizations, we compute the ensemble average over Δ values given δ , denoted $\langle T(\Delta, \delta) \rangle_\Delta$, which is shown in black squares. It matches the capillary time scale $T_2(\delta)$, i.e., the typical capillary time at the

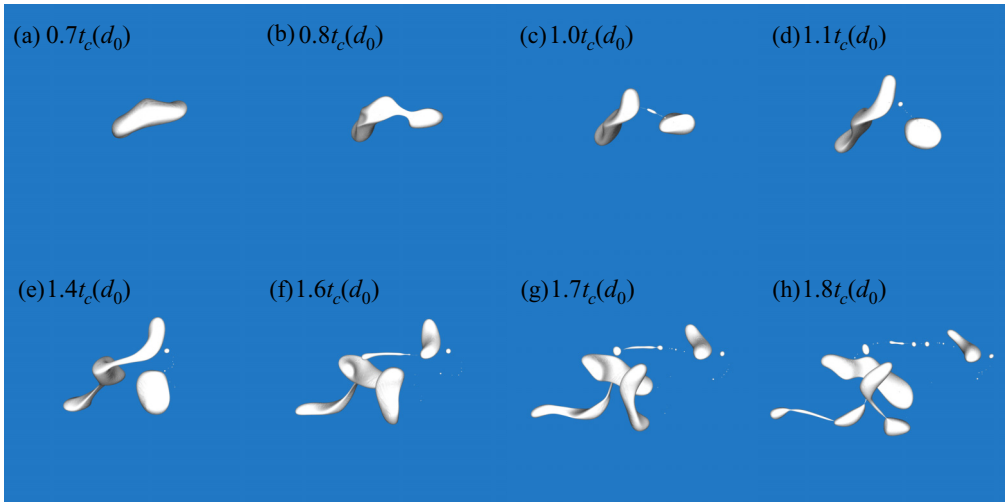


FIG. 2. DNS snapshots of a typical breakup sequence, with the initial bubble size $d_0/d_h = 2.9$. The bubbles' interface is represented in white. The first images (a), (b) show large-scale deformation due to turbulence, happening over the eddy turn over time at the size of the initial bubble scale d_0 , $t_c(d_0) = \epsilon^{-1/3} d_0^{2/3}$, leading (c), (d) to the formation of thin filaments. (e)–(h) Successive splitting events of the filament are visible leading to multiple child bubbles. The filaments quickly break creating a wide range of bubble sizes, the smallest being orders of magnitude smaller than the initial one.

length δ (shown in black dashed line), up to $\delta = d_h$, without any adjustable parameters. However, a broad distribution of timescale is observed, and the standard deviation of the bubble lifetime is barely defined, which cannot be explained by a simple Rayleigh-Plateau instability of a single bubble filament of diameter δ . The dispersion of the individual splitting times can be attributed to the various shapes induced by the turbulent flow and more generally to the inherent stochasticity of the breakup events. To our knowledge, the Rayleigh-Plateau instability dynamics for a gas filament in presence of an external noise has never been investigated. A recent study on liquid filament [44] has shown that indeed, initial noise on the filament shape induces a widening of the satellite drop size distribution. The velocity fluctuations associated with the turbulent flow around the bubble could also play a crucial role by inducing various filament shapes. However, a recent study by the same authors [35] showed that for the final stage of evolution, i.e., the pinch-off of a single bubble in a turbulent flow, the shrinking dynamics of the bubble neck is only slightly modified compared with the quiescent case. Determining how the growth rate of RP instability would be modified by the variety of filament shapes and by the presence of the flow will require further investigations. For $\delta > d_h$, the breakup time seems to converge to a value independent of δ . We have also separately verified that, $\langle T(\Delta, \delta) \rangle$ being a function of two variables, the ensemble average of over δ values for a given Δ , $\langle T(\Delta, \delta) \rangle_\delta$ is independent of Δ . This confirms the scaling proposed in Eq. (5).

IV. EXPERIMENTAL VALIDATION

We now aim to verify that an initial large separation of scales, namely for which $d_0/d_h \ll 1$, indeed leads to a universal $\mathcal{N}(d) \propto d^{-3/2}$ in the sub-Hinze-scale regime. We will analyze laboratory and numerical data of bubble size distribution under breaking waves from previous work [18,22]. On top of this, we compare the results to a more idealized configuration consisting of a single large bubble injected in a turbulent flow, both numerically [39] and experimentally.

We design an experiment to inject a unique large air cavity (bubble) of initial size much larger than the Hinze scale d_h . Using a thin latex membrane, we pressurize an underwater air cavity of

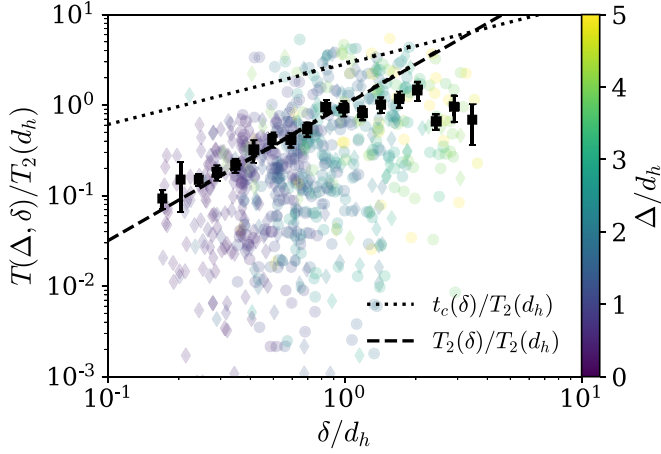


FIG. 3. Lifetime of bubbles as a function of the size of the smallest bubble they split apart into. The size of the parent bubble is given by the color. Most splitting events occur on a timescale faster than the eddy turnover time $t_c(\delta)$, shown in dotted line, suggesting that the splitting events are not primarily instigated by turbulent deformations at the small child bubble size. The ensemble averaged time $\langle T(\Delta, \delta) \rangle_\Delta$ is shown in black squares and follows the capillary timescale of the small child bubble $T_2(\delta)$ without any adjusting parameters (shown as the dashed line). Diamonds and circles denote two levels of resolution, associated with a grid size of $\ell = 0.0075d_0$ and $\ell = 0.015d_0$, respectively, with d_0 the initial bubble size.

diameter $d_0 = 40$ mm, as shown in Fig. 4(a). In the water phase, a turbulent flow is generated in a horizontal middle plane located above the initial air pocket, similarly to Ref. [35]. It is done by arranging and running four pumps pointing toward the center. The resulting velocity field is characterized using a particle image velocimetry algorithm [45], which gives $u' = 0.25$ m/s, $L_{\text{int}} = 15$ mm, $\epsilon = 0.7$ m² s⁻³ and $Re_\lambda = 340 \pm 40$, where u' is the root mean squared (rms) velocity,

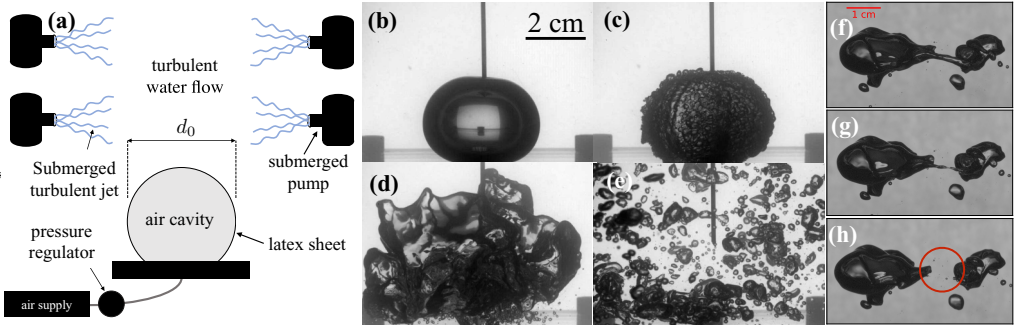


FIG. 4. (a) Sketch of the experimental setup. (b)–(e) Successive snapshots of the release of a large bubble into a turbulent background flow. (b) Before the crack opening, an air pocket is trapped within an extended thin rubber sheet. (c) Just after the membrane piercing, the membrane moves away, generating locally a high shear situation, but on a timescale much shorter than the typical turbulence time at the bubble scale (0.2 ms). (d) The small wavelength disturbances are then dissipated by viscosity while the interface deforms at larger scale under the action of the background turbulence. (e) Eventually the bubble interface experiences multibreaking events, generating a broad distribution of bubble size. (f)–(h) Zoom in view of a typical breaking dynamics of a gas filament during the process. The time between images is 2 ms. The red rectangle highlights the region where ligament collapsed creating many sub-Hinze bubbles.

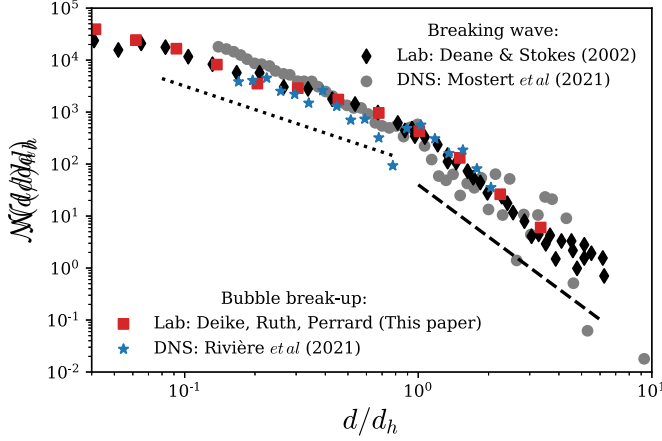


FIG. 5. Bubble size distribution obtained both experimentally and numerically in two different geometries: a breaking wave (\blacklozenge , \bullet) and a single bubble breaking (\blacksquare , \star). The distribution exhibits two power laws: for $d > d_h$, $\mathcal{N}(d) \propto d^{-10/3}$ (dashed line), while $\mathcal{N}(d) \propto d^{-3/2}$ for $d < d_h$ (dotted line).

L_{int} the integral length scale and Re_λ is the Taylor Reynolds number that characterizes the turbulent velocity fluctuations. These set the Hinze scale to $d_h \approx 4.8$ mm with $\gamma = 50$ mN/m and $\rho = 10^3$ kg/m³. The ratio between the initial cavity diameter $d_0 = 40$ mm and the Hinze scale is therefore $d_0/d_h = 8.3$, which defines a Weber number $We = We_c(d_0/d_h)^{5/3} \approx 100$, corresponding to a large separation of scales. Note that in the literature We_c varies between 1 and 5, depending on the details of the turbulence setup [13–15]. We consider $We_c = 3$ for consistency with the DNS [39]. The air pocket is released by piercing the membrane, which triggers a rapid crack opening. After a transient regime of interface deformations by interfacial instabilities, the bubble rises and deforms under the combined action of buoyancy and turbulent background flow. A comparison with the quiescent case shows that the bubble fragments are mainly produced by the turbulent background flow. In the main turbulent region located between the four pumps, a broad range of bubble sizes is eventually generated, as illustrated by the successive snapshots of Figs. 4(b)–4(e). The large air bubbles are highly deformed and lead to the formation of tiny air filaments, breaking down in small bubbles as illustrated in Figs. 4(f)–4(h). To measure the size distribution quantitatively, we move the pumps 20 cm above the air pocket. We then process images taken with a high-speed camera with a resolution of 15 μm per pixel filming at 1000 fps to compute the distribution of bubble sizes in the region of the most intense turbulence. We compute the bubble size distribution averaged over two runs and 1.2 s $\approx 20 T_{\text{int}}$ each after the first breakup, with $T_{\text{int}} = L_{\text{int}}/u'$ the integral timescale associated with the correlation time of the largest eddies.

Figure 5 shows the bubble size distributions $\mathcal{N}(d)$ obtained under breaking waves [18,22] and from a single large bubble breaking in a turbulent flow, both experimentally and numerically. Within all four data sets, for $d > d_h$, the distributions exhibit $\mathcal{N}(d) \propto d^{-10/3}$ scaling, in agreement with other previous experimental measures below a breaking wave [17,19,20] and in agreement with the classic breakup cascade argument from Garrett *et al.* [24].

For $d < d_h$, all four dataset also exhibit $\mathcal{N}(d) \propto d^{-3/2}$ across a large range of scales. The bubble size distribution measured under breaking waves is in close agreement with the data obtained from single bubble breakup in turbulence, suggesting that the same underlying mechanisms are at play for the sub-Hinze bubble production outside if laboratory experiments. This result also justifies that $F(\Delta, \delta) = F(\Delta)$. Indeed, since $\mathcal{N}(d) \propto d^{-3/2}$, the left-hand side of Eq. (8) is proportional to $d^{-3/2}$ and since, from the time analysis the d dependency of the right-hand side is $d^{-3/2}F(\Delta, \delta)$, one gets *a posteriori* that $F(\Delta, \delta)$ must be independent of δ .

V. CONCLUSION

The observed size distribution, considered alongside the mechanism we present for sub-Hinze bubble production, suggests that, for these experimental cases, the production rate of sub-Hinze scale bubbles is controlled by surface tension through the breaking dynamics of gas filaments. It extends to sub-Hinze bubble production the framework of Villiermaux [34], who stated that, for liquids, ligaments may universally control fragmentation processes. Contrary to many fragmentation processes in which a physical length scale sets the average fragmentation size, there is no such specific length scale, and a power-law distribution is observed instead. These capillary effects only dominate the production of sub-Hinze bubbles, since for larger bubbles, the dynamics, and thereby the lifetime, of the parent bubbles can also be controlled by the eddy turnover time.

To summarize, the scaling for $d > d_h$ [18] reads

$$\mathcal{N}(d, t) = Q\epsilon^{-1/3}d^{-10/3} \text{ for } d > d_h, \quad (12)$$

where Q is the volume of air injected to the breaking cascade per volume of water per second, and can be evaluated from the breaker geometry and energetics [21,22]. The prefactor for the sub-Hinze distribution can then be evaluated using the continuity of \mathcal{N} at d_h , and

$$\mathcal{N}(d, t) = Q\left(\frac{We_c \gamma}{2\rho}\right)^{-11/10} \epsilon^{2/5} d^{-3/2} \text{ for } d < d_h. \quad (13)$$

In summary, when $d_0 \gg d_h$, large-scale inertial breakups and small-scale capillary splitting events occur concurrently. The background turbulence sets the geometry of each breakup event over a time $t_c(\Delta)$ and then freezes relative to the capillary timescale [35], over which a cascade of small-scale splitting events occur. The classic turbulent inertial breakup scenario [Eq. (12)] combined with the capillary driven fragmentation regime [Eq. (13)] provides a physical explanation for the entirety of the bubble size distribution when large air cavities break apart under the action of turbulence.

ACKNOWLEDGMENTS

This work was supported by the NSF CAREER Award No. 1844932 to L.D. A.R. was supported by an International Fund grant from Princeton University to L.D. S.P. and A.R. were supported by the Labex ENS-ICFP. Computations were performed on the Princeton supercomputer Tiger2, as well as on Stampede, through XSEDE allocations to L.D. and W.M., XSEDE is an NSF funded program 1548562. We would like to acknowledge high-performance computing support from Cheyenne [46] provided by NCAR's Computational and Information Systems Laboratory, sponsored by the National Science Foundation.

-
- [1] F. R. Keeling, On the role of large bubbles in air-sea gas exchange and supersaturation in the ocean, *J. Mar. Res.* **51**, 237 (1993).
 - [2] L. Deike and W. K. Melville, Gas transfer by breaking waves, *Geophys. Res. Lett.* **45**, 10 (2018).
 - [3] B. G. Reichl and L. Deike, Contribution of sea-state dependent bubbles to air-sea carbon dioxide fluxes, *Geophys. Res. Lett.* **47**, e2020GL087267 (2020).
 - [4] T. G. Leighton, D. G. H. Coles, M. Srokosz, P. R. White, and D. K. Woolf, Asymmetric transfer of CO_2 across a broken sea surface, *Sci. Rep.* **8**, 1 (2018).
 - [5] D. Atamanchuk, J. Koelling, U. Send, and D. W. R. Wallace, Rapid transfer of oxygen to the deep ocean mediated by bubbles, *Nat. Geosci.* **13**, 232 (2020).
 - [6] E. D. Spiel and G. De Leeuw, Formation and production of sea spray aerosol, *J. Aerosol Sci.* **27**, S65 (1996).

- [7] E. Ghabache, A. Antkowiak, C. Josserand, and T. Séon, On the physics of fizziness: How bubble bursting controls droplets ejection, *Phys. Fluids* **26**, 121701 (2014).
- [8] L. Deike, E. Ghabache, G. Liger-Belair, A. K. Das, S. Zaleski, S. Popinet, and T. Séon, Dynamics of jets produced by bursting bubbles, *Phys. Rev. Fluids* **3**, 013603 (2018).
- [9] A. Berny, L. Deike, T. Séon, and S. Popinet, Role of all jet drops in mass transfer from bursting bubbles, *Phys. Rev. Fluids* **5**, 033605 (2020).
- [10] S. Galinat, O. Masbernat, P. Guiraud, C. Dalmazzone, C. Noi *et al.*, Drop break-up in turbulent pipe flow downstream of a restriction, *Chem. Eng. Sci.* **60**, 6511 (2005).
- [11] B. Gopalan and J. Katz, Turbulent Shearing of Crude Oil Mixed with Dispersants Generates Long Microthreads and Microdroplets, *Phys. Rev. Lett.* **104**, 054501 (2010).
- [12] N. Afshar-Mohajer, C. Li, A. M. Rule, J. Katz, and K. Koehler, A laboratory study of particulate and gaseous emissions from crude oil and crude oil-dispersant contaminated seawater due to breaking waves, *Atmos. Environ.* **179**, 177 (2018).
- [13] F. Risso and J. Fabre, Oscillations and breakup of a bubble immersed in a turbulent field, *J. Fluid Mech.* **372**, 323 (1998).
- [14] C. Martínez-bazán, J. L. Montanes, and J. C. Lasheras, On the breakup of an air bubble injected into a fully developed turbulent flow. Part 1. Breakup frequency, *J. Fluid Mech.* **401**, 157 (1999).
- [15] B. Lalanne, O. Masbernat, and F. Risso, A model for drop and bubble breakup frequency based on turbulence spectra, *AIChE J.* **65**, 347 (2019).
- [16] Y. Qi, M. M. A. Ullah, and R. Ni, Towards a model of bubble breakup in turbulence through experimental constraints, *Int. J. Multiphase Flow* **132**, 103397 (2020).
- [17] M. R. Loewen, M. A. O'Dor, and M. G. Skafel, Bubbles entrained by mechanically generated breaking waves, *J. Geophys. Res.* **101**, 20759 (1996).
- [18] G. B. Deane and M. D. Stokes, Scale dependence of bubble creation mechanisms in breaking waves, *Nature (London)* **418**, 839 (2002).
- [19] G. Rojas and M. R. Loewen, Fiber-optic probe measurements of void fraction and bubble size distributions beneath breaking waves, *Exp. Fluids* **43**, 895 (2007).
- [20] C. E. Blenkinsopp and J. R. Chaplin, Bubble size measurements in breaking waves using optical fiber phase detection probes, *IEEE J. Oceanic Eng.* **35**, 388 (2010).
- [21] L. Deike, W. K. Melville, and S. Popinet, Air entrainment and bubble statistics in breaking waves, *J. Fluid Mech.* **801**, 91 (2016).
- [22] W. Mostert, S. Popinet, and L. Deike, High-resolution direct simulation of deep water breaking waves: Transition to turbulence, bubbles and droplets production, *J. Fluid Mech.* **942**, A27 (2022).
- [23] W. H. R. Chan, P. L. Johnson, P. Moin, and J. Urzay, The turbulent bubble break-up cascade. Part 2. Numerical simulations of breaking waves, *J. Fluid Mech.* **912**, A43 (2021).
- [24] C. Garrett, M. Li, and F. Farmer, The connection between bubble size spectra and energy dissipation rates in the upper ocean, *J. Phys. Oceanogr.* **30**, 2163 (2000).
- [25] S. B. Pope, *Turbulent Flows* (Cambridge University Press, Cambridge, UK, 2000).
- [26] A. N. Kolmogorov, The local structure of turbulence in incompressible viscous fluid for very large Reynolds numbers, *Cr Acad. Sci. URSS* **30**, 301 (1941).
- [27] J. O. Hinze, Fundamentals of the hydrodynamic mechanism of splitting in dispersion processes, *AIChE J.* **1**, 289 (1955).
- [28] C. Martínez-bazán, J. Rodríguez-Rodríguez, G. Deane, J. L. Montañes, and J. C. Lasheras, Considerations on bubble fragmentation models, *J. Fluid Mech.* **661**, 159 (2010).
- [29] Jiří Vejražka, M. Zednikova, and P. Stanovsky, Experiments on breakup of bubbles in a turbulent flow, *AIChE J.* **64**, 740 (2018).
- [30] N. S. Ethier and T. G. Kurtz, *Markov Processes: Characterization and Convergence* (John Wiley & Sons, New Jersey, 2009), Vol. 282.
- [31] D. Ramkrishna, *Population Balances. Theory and Application to Particular Systems in Engineering* (Academic Press, San Diego, 2000).
- [32] Y. Liao and D. Lucas, A literature review of theoretical models for drop and bubble breakup in turbulent dispersions, *Chem. Eng. Sci.* **64**, 3389 (2009).

- [33] T. Wang, J. Wang, and Y. Jin, A novel theoretical breakup kernel function for bubbles/droplets in a turbulent flow, *Chem. Eng. Sci.* **58**, 4629 (2003).
- [34] E. Villermaux, Fragmentation versus cohesion, *J. Fluid Mech.* **898**, P1 (2020).
- [35] D. Ruth, W. Mostert, S. Perrard, and L. Deike, Bubble pinch-off in turbulence, *Proc. Natl. Acad. Sci. USA* **116**, 25412 (2019).
- [36] H. Lamb, *Hydrodynamics*, 6th ed. (Cambridge University Press, Cambridge, UK, 1995).
- [37] S. Popinet, An accurate adaptive solver for surface-tension-driven interfacial flows, *J. Comput. Phys.* **228**, 5838 (2009).
- [38] S. Popinet, Numerical models of surface tension, *Annu. Rev. Fluid Mech.* **50**, 49 (2018).
- [39] A. Rivi re, W. Mostert, S. Perrard, and L. Deike, Sub-Hinze scale bubble production in turbulent bubble break-up, *J. Fluid Mech.* **917**, A40 (2021).
- [40] C. Rosales and C. Meneveau, Linear forcing in numerical simulations of isotropic turbulence: Physical space implementations and convergence properties, *Phys. Fluids* **17**, 095106 (2005).
- [41] S. Perrard, A. Rivi re, W. Mostert, and L. Deike, Bubble deformation by a turbulent flow, *J. Fluid Mech.* **920**, A15 (2021).
- [42] D. B. Allan, T. Caswell, N. C. Keim, and C. M. van der Wel, soft-matter/trackpy: Trackpy v0.4.2 (2019).
- [43] J. C. Crocker and D. G. Grier, Methods of digital video microscopy for colloidal studies, *J. Colloid Interface Sci.* **179**, 298 (1996).
- [44] S. Pal, D. Fuster, M. Cialesi-Esposito, and S. Zaleski, Statistics of drops generated from ensembles of randomly corrugated ligaments, [arXiv:2106.16192v2](https://arxiv.org/abs/2106.16192v2).
- [45] W. Thielicke and E. Stamhuis, Pivlab–towards user-friendly, affordable and accurate digital particle image velocimetry in matlab, *J. Open Res. Softw.* **2**, e30 (2014).
- [46] Doi: [10.5065/D6RX99HX](https://doi.org/10.5065/D6RX99HX).